



## Can grain size sensitive flow lubricate faults during the initial stages of earthquake propagation?

This is the peer reviewed version of the following article:

*Original:*

De Paola, N., Holdsworth, R.E., Viti, C., Collettini, C., Bullock, R. (2015). Can grain size sensitive flow lubricate faults during the initial stages of earthquake propagation?. EARTH AND PLANETARY SCIENCE LETTERS, 431, 48-58 [10.1016/j.epsl.2015.09.002].

*Availability:*

This version is available <http://hdl.handle.net/11365/982357> since 2017-05-19T11:46:58Z

*Published:*

DOI:10.1016/j.epsl.2015.09.002

*Terms of use:*

Open Access

The terms and conditions for the reuse of this version of the manuscript are specified in the publishing policy. Works made available under a Creative Commons license can be used according to the terms and conditions of said license.

For all terms of use and more information see the publisher's website.

(Article begins on next page)

1 **Can grain size sensitive flow lubricate faults during the initial stages of earthquake**  
2 **propagation?**

3 Nicola De Paola<sup>a\*</sup>, Robert E. Holdsworth<sup>a</sup>, Cecilia Viti<sup>b</sup>, Cristiano Collettini<sup>c,d</sup>, Rachael  
4 Bullock<sup>a</sup>.

5 <sup>(a)</sup>Rock Mechanics Laboratory, Earth Sciences Department, Durham University, South Road,  
6 Durham, DH1 3LE, UK.

7 <sup>(b)</sup>Dipartimento di Scienze Fisiche, della Terra e dell' Ambiente, Siena University, Via  
8 Laterina 8, 53100 Siena, Italy.

9 <sup>(c)</sup>Dipartimento di Scienze della Terra, Sapienza Università di Roma, Piazzale Aldo Moro, 5 –  
10 00185 Roma, Italy.

11 <sup>(d)</sup>Istituto Nazionale di Geofisica e Vulcanologia, Sezione Roma 1, Via Vigna Murata 605, I-  
12 00143 Rome, Italy.

13 \*Corresponding Author: Nicola De Paola, Rock Mechanics Laboratory, Earth Sciences  
14 Department, Durham University, South Road, Durham, DH1 3LE, UK.

15 Tel. +44 (0)191 3342333. E-mail: nicola.de-paola@durham.ac.uk.

16 **Abstract**

17 Recent friction experiments carried out under upper crustal P-T conditions have shown that  
18 microstructures typical of high temperature creep develop in the slip zone of experimental  
19 faults. These mechanisms are more commonly thought to control aseismic viscous flow and  
20 shear zone strength in the lower crust/upper mantle. In this study, displacement-controlled  
21 experiments have been performed on carbonate gouges at seismic slip rates ( $1 \text{ ms}^{-1}$ ), to  
22 investigate whether they may also control the frictional strength of seismic faults at the higher  
23 strain rates attained in the brittle crust. At relatively low displacements ( $< 1 \text{ cm}$ ) and  
24 temperatures ( $\leq 100 \text{ }^\circ\text{C}$ ), brittle fracturing and cataclasis produce shear localisation and grain  
25 size reduction in a thin slip zone ( $150 \text{ }\mu\text{m}$ ). With increasing displacement (up to  $15 \text{ cm}$ ) and

26 temperatures ( $T$  up to  $600\text{ }^{\circ}\text{C}$ ), due to frictional heating, intracrystalline plasticity mechanisms  
27 start to accommodate intragranular strain in the slip zone, and play a key role in producing  
28 nanoscale subgrains ( $\leq 100\text{ nm}$ ). With further displacement and temperature rise, the onset of  
29 weakening coincides with the formation in the slip zone of equiaxial, nanograin aggregates  
30 exhibiting polygonal grain boundaries, no shape or crystal preferred orientation and low  
31 dislocation densities, possibly due to high temperature ( $> 900\text{ }^{\circ}\text{C}$ ) grain boundary sliding  
32 (GBS) deformation mechanisms. The observed micro-textures are strikingly similar to those  
33 predicted by theoretical studies, and those observed during experiments on metals and fine-  
34 grained carbonates, where superplastic behaviour has been inferred. To a first approximation,  
35 the measured drop in strength is in agreement with our flow stress calculations, suggesting  
36 that strain could be accommodated more efficiently by these mechanisms within the weaker  
37 bulk slip zone, rather than by frictional sliding along the main slip surfaces in the slip zone.  
38 Frictionally induced, grainsize-sensitive GBS deformation mechanisms can thus account for  
39 the self-lubrication and dynamic weakening of carbonate faults during earthquake propagation  
40 in nature.

41 **Keywords:** Earthquake, Grain Boundary Sliding, Superplasticity, Friction, Viscous Flow,  
42 Dynamic Weakening.

### 43 **1. Introduction**

44 Earthquakes are typically hosted in the shallower portion of crustal fault zones ( $\leq 15\text{ km}$   
45 depth and ambient  $T \leq 300\text{ }^{\circ}\text{C}$ ), where fracturing and cataclasis are traditionally thought to be  
46 the dominant processes during frictional sliding (Kohlstedt et al., 1995; Scholz, 1998; Sibson,  
47 1977). At greater depths and temperatures, in the lower crust/upper mantle, viscous flow,  
48 potentially associated with superplastic behaviour (Ashby and Verrall, 1973; Boullier and  
49 Gueguen, 1975; Hiraga et al., 2010; Rutter et al., 1994; Schmid et al., 1977; Walker et al.,  
50 1990), is inferred to facilitate aseismic creep along shear zones, based on experimental data

51 and microstructural observations (Ashby, 1977; Kohlstedt et al., 1995; Passchier, 2005;  
52 Poirier, 1985; Rutter, 1995, 1999). Grain boundary sliding (GBS) diffusion creep, associated  
53 with superplastic behaviour, i.e., the ability of materials to achieve unusually high elongations  
54 ( $> 100\%$ ) before failure, has been observed at high strain rates ( $> 10^2 \text{ s}^{-1}$ ) for a range of nano-  
55 phase alloys (Chandra, 2002) and ceramics (Lankford, 1996). These mechanisms could  
56 potentially occur in ultrafine-grained (nano-scale) geological materials deformed at higher  
57 strain rates and temperatures appropriate for seismic slip or slow earthquakes (Green et al.,  
58 2015; Rutter and Brodie, 1988; Schubnel et al., 2013; Verberne et al., 2014).

59 Recent laboratory experiments, performed using rotary shear apparatuses, show that when  
60 sliding at seismic velocities ( $\geq 0.5 \text{ ms}^{-1}$ ) the frictional strength of faults,  $\mu$ , is significantly  
61 lower ( $\mu = 0.1-0.3$ ) (Di Toro et al., 2011; Goldsby and Tullis, 2011; Hirose and Shimamoto,  
62 2005; Reches and Lockner, 2010) than when sliding at low ( $< 1 \text{ mms}^{-1}$ ), sub-seismic speeds  
63 ( $\mu = 0.6-0.85$ ) (Byerlee, 1978). Understanding the processes controlling the evolution of fault  
64 strength as seismic slip rates are approached is of paramount importance. Strength cannot be  
65 measured directly using seismological data, yet it affects the magnitude of the stress drop, the  
66 heat flow signature of seismogenic faults, and the relative partitioning of the earthquake  
67 energy budget (i.e., the proportion of energy dissipated as seismic waves that can travel to the  
68 Earth's surface and cause damaging earthquakes). It has been proposed that slip weakening of  
69 experimental and natural seismic faults is caused by thermally-activated processes triggered  
70 by localised frictional heating and high temperatures attained in the slip zone (Rice, 2006).  
71 Furthermore, recent studies show that cohesive slip zones (SZs), in natural (Siman-Tov et al.,  
72 2013) and experimental carbonate seismic faults (De Paola et al., 2011; Fondriest et al., 2013;  
73 Green et al., 2015; Ree et al., 2014; Smith et al., 2013; Verberne et al., 2014), are composed  
74 of striated and mirrored slip surfaces (SSs). Microstructural analyses show that the SSs and  
75 the adjacent SZ material are made of calcite nanograin ( $D < 1 \text{ }\mu\text{m}$ ) aggregates with a



76 polygonal texture, a microstructure consistent with deformation by creep deformation  
77 mechanisms. The use of mirror SSs and nano-granular SZ textures as indicators of seismic  
78 slip on faults in carbonates (e.g. Ree et al., 2014; Smith et al., 2013) has been questioned by  
79 Verberne et al. (2013, 2014) who have shown that similar features can develop during low  
80 velocity ( $1 \mu\text{ms}^{-1}$ ) friction experiments performed on simulated calcite gouge at upper crustal  
81 P-T conditions. However, the grain-scale processes suggested to account for the observed  
82 weakening of rocks deformed in the laboratory at seismic velocities are still debated (De  
83 Paola et al., 2011; De Paola, 2013; Han et al., 2010; Tisato et al., 2012), as is their occurrence  
84 along natural faults during earthquake propagation. Verberne et al. (2014) performed  
85 microstructural analyses on experimentally deformed samples at sub-seismic slip rates ( $1$   
86  $\mu\text{ms}^{-1}$ ) and low temperatures ( $<140 \text{ }^\circ\text{C}$ ). They show that nanofiber formation during  
87 nanogranular flow with diffusive mass transfer can promote velocity-weakening behaviour  
88 and earthquake nucleation in carbonate rocks. Green et al. (2015) integrated microstructural  
89 observations and experimental work to show that mineral phase transformation in carbonate  
90 rocks, occurring at the high temperatures produced by frictional heating, can generate  
91 nanometric materials which are weak at seismic slip rates ( $\approx 1 \text{ ms}^{-1}$ ) and flow by grain-  
92 boundary sliding mechanisms.

93 Here we study the evolution of deformation mechanisms, and their control on the frictional  
94 strength of slip zones developed in simulated, carbonate gouges during accelerating sliding to  
95 seismic slip rates ( $v = 1 \text{ ms}^{-1}$ ). To do so we combine results from new laboratory friction  
96 experiments with microstructural observations on samples sheared up to the attainment of  
97 dynamic weakening, but *prior* to the onset of phase transformation. Flow stress calculations  
98 are performed to investigate whether grain-size-sensitive creep deformation mechanisms,  
99 potentially associated with superplastic behaviour, can effectively weaken faults and facilitate  
100 earthquake propagation in the shallow crust. To illustrate the relevance of our findings to

101 natural faults, we also carried out microstructural observations on the principal slip zone  
102 material extracted from natural, seismically active faults in carbonates.

## 103 **2. Experimental settings**

104 Friction experiments were performed in the Rock Mechanics Laboratory, at Durham  
105 University (UK), using a low to high velocity rotary shear apparatus (details in  
106 Supplementary Information 1 – Figure SI1) built by the Marui & Co., Ltd Company (Osaka,  
107 Japan). We performed a set of eight displacement-controlled experiments at room temperature  
108 and humidity conditions on fine-grained ( $63 < D < 93 \mu\text{m}$ ), carbonate gouges at target slip  
109 rates  $v = 1 \text{ ms}^{-1}$  and normal  $\sigma_n = 12\text{-}18 \text{ MPa}$  (Supplementary Information – Table I). During  
110 displacement-controlled experiments, arrested at pre-determined displacements, the electric  
111 servomotor of the apparatus was controlled in the digital mode, using a signal generator  
112 DF1906 (NF corporation) (Supplementary Information 1).

113 A synthetic fault zone was created by sandwiching 2 g of simulated fault gouge between  
114 two stainless steel cylinders (25 mm in diameter), whose ends were machined with radial  
115 grooves 500  $\mu\text{m}$  high to grip the sample surface (Supplementary Information 1 – Figure SI2).  
116 The experiments were run under drained conditions, and to limit gouge loss during the  
117 experiments, the sample assembly was confined using a Teflon ring. Teflon rings were cut  
118 and tightened onto the stainless steel cylinder using a hose clamp. The inner edges of the rings  
119 were machined to reduce their sharpness, and thus avoid ring damage and sample  
120 contamination by Teflon during the insertion of the stainless steel cylinders (Supplementary  
121 Information 1 – Figure SI2).

122 Samples were recovered after each experiment to study the slip zone microstructures. Thin  
123 sections for optical microscope observations were taken from slices of the slip zone cut at  $2/3$   
124 of the radius, to make observations consistent with calculated values of the velocity,  $v$ , and  
125 the displacement  $d$  (Supplementary Information 2).

### 126 3. Mechanical data

127 To identify the mechanisms controlling the evolution of friction, we performed a set of  
128 displacement-controlled experiments, with a target speed  $v = 1 \text{ ms}^{-1}$ , normal stresses  $\sigma_n = 12$ -  
129 18 MPa, and arrested at displacements  $d$  from 0.007 to 1.46 m (Supplementary Information  
130 Table I). Experiments arrested at different displacements show similar acceleration paths (Fig.  
131 1a-b), showing that the conditions during our experiments are reproducible (Fig. 1c-d). It also  
132 means that microstructures developed at different stages/displacements can be used to study  
133 the evolution of deformation mechanisms in the slip zone, and how these may affect frictional  
134 strength evolution.

135 During experiments run up to 1.44 - 1.46 m total slip, the imposed target speed of  $1 \text{ ms}^{-1}$   
136 was attained after 0.12 m of slip (Figs. 1a-b). The measured strength consistently showed a  
137 four stage evolution (e.g. Exp. Du304-307 in Figs. 1c-d, Supplementary Information Table I):  
138 Stage I) attainment of initial friction values,  $\mu_i = 0.67$ , upon instantaneous acceleration toward  
139 target speed; Stage II) increase in friction up to peak values  $\mu_p = 0.80$ – $0.88$ , attained just  
140 before acceleration to target speed was complete; Stage III) sudden decrease in friction to low  
141 steady-state values,  $\mu_{ss} = 0.17$ - $0.21$ , attained during sliding at constant velocity  $v = 1 \text{ ms}^{-1}$ ; and  
142 Stage IV) sudden increase of friction to  $\mu_f = 0.44$  -  $0.45$ , observed upon deceleration of the  
143 motor.

144 The temperature rise produced during the laboratory experiments has been estimated, to a  
145 first approximation, using (Rice, 2006)

$$146 \Delta T = \frac{\mu \sigma_n \sqrt{v d}}{\rho c_p \sqrt{\pi \kappa}} \quad \text{Eq. 1}$$

147 where  $\mu$  represents the friction coefficient,  $\sigma_n$  is the normal stress,  $d$  is the displacement,  $\rho$  is  
148 the rock density,  $c_p$  is the specific heat capacity and  $\kappa$  is the thermal diffusivity.  
149 Microstructural evidence for slip localisation within slip zones with thickness  $h < 150 \text{ }\mu\text{m}$   
150 satisfies the condition  $h \leq 4\sqrt{\kappa d/v}$ , which allows to treat the slip zone as a plane of zero

151 thickness and account for heat diffusion using Eq. 1. For experiments in which steady-state  
152 conditions were attained (e.g., Du304 and Du307 in Fig. 1c-d), temperatures were calculated  
153 up to the displacements,  $d_{tr}$ , attained at the end of the steep drop in friction observed during  
154 the transient stage of friction evolution to low, steady-state values, e.g., at  $d_{tr} = 0.23-0.08$  m  
155 (Table I). The contribution to temperature increase by sliding from peak friction values to  
156 those attained at  $d_{tr}$  was calculated by using the mean value for  $\mu$  in Eq. 1. The following  
157 physical properties of calcite, the main mineralogical component in the deformed rocks, were  
158 used for temperature calculations:  $\rho = 2700$  kg/m<sup>3</sup>,  $\kappa = 1.48 \cdot 10^{-6}$  m<sup>2</sup>s<sup>-1</sup> and  $c_p = 700$  J kg<sup>-1</sup> °K<sup>-1</sup>  
159 (Di Toro et al., 2011 and references therein). The mechanical parameters  $d$ ,  $\mu$ ,  $\sigma_n$  and  $v$  used  
160 for the temperature calculations are those reported in Supplementary Information Table I, and  
161 the temperatures calculated by Eq. 1 are plotted vs. the measured friction coefficients in Fig.  
162 2. It is observed that friction values are in accord with the range of values predicted by  
163 Byerlee's rule for temperatures  $\leq 554$  °C ( $\mu_f = 0.68-0.80$ ), but significantly lower ( $\mu_{ss} = 0.17-$   
164  $0.21$ ) when  $T \geq 979$  °C (Fig. 2).

#### 165 **4. Microstructural Observations and Interpretations**

##### 166 **4.1 Experimental faults**

167 Samples deformed during Stage I ( $d = 0.007-0.09$  m, Fig. 1c-d) show the formation of an  
168 irregular slip zone (SZ) and rough slip surface (SS), due to the presence of grooves (up to 25  
169  $\mu$ m wide) and ridges, oriented parallel to the slip direction (Fig. 3a). A sharply defined,  
170 irregular slip surface (SS) bounds the upper part of the SZ, showing variable thickness (20-  
171 200  $\mu$ m), whilst the lower bound between the SZ and less deformed material is sharp, but  
172 rather irregular and wavy (Fig. 3b). The SS is heterogeneous, displaying smooth compact  
173 areas interspersed with more granular porous areas (Fig. 3a). The granular portions of the SS  
174 appear to be coarser in grain size ( $10 < D < 25$   $\mu$ m) compared to the smooth regions. The  
175 smooth portions of the SS are made of fine-grained clasts ( $1 < D < 5$   $\mu$ m), which are sharply

176 truncated against the SS (Fig. 3c). The shape of the clasts on the SS and in the SZ below the  
177 SS, is typically angular to sub-angular (Fig. 3c). In places, the smaller clasts display a sub-  
178 rounded shape. In the smooth and compact patches, the SS and SZ are still porous, but the  
179 porosity, like the grain size, seems finer. Overall, the SZ contains coarse- and fine-grained ( $1$   
180  $< D < 5 \mu\text{m}$ ), angular clasts, likely formed by brittle fracturing and cataclasis during frictional  
181 sliding at low temperatures  $< 100 \text{ }^\circ\text{C}$  (Fig. 2).

182 During Stage II, samples show the development of a cohesive SZ,  $< 150 \mu\text{m}$  thick (Fig. 4a),  
183 containing multiple SSs sandwiching thin layers (tl,  $\approx 5 \mu\text{m}$ ) of sub-rounded nanograins (Fig.  
184 4b-c). TEM analyses show that tl contain slightly larger clasts of calcite ( $D \leq 1 \mu\text{m}$ ) dispersed  
185 within a porous assemblage of calcite nanograins,  $\leq 100 \text{ nm}$  in size, with sub-rounded crystal  
186 shapes (Fig. 4d). The calcite clasts host dislocations, locally arranged to form dislocation  
187 walls separating subgrains ( $D \leq 100 \text{ nm}$ ) with small angular misorientations; this is typical of  
188 low temperature ( $\leq 600 \text{ }^\circ\text{C}$ ) intragranular dislocation creep deformation (Rutter, 1995) (Fig.  
189 4d). Bright-field TEM images show that, together with dislocation walls and subgrain  
190 boundaries, calcite clasts (CC) exhibit “damaged” rims, hosting rounded bubbles and lobate,  
191 low-contrast features (Fig. 4e). These nanostructures suggest concomitant decarbonation and  
192 amorphization processes, preferentially located within the strained calcite rims and at  
193 subgrain boundaries. This is where crystal structure defects are concentrated and where, it is  
194 suggested, calcite becomes more reactive. We propose that the occurrence of an amorphous  
195 phase along subgrain boundaries will facilitate clast disaggregation and the subsequent  
196 formation of nano-sized, calcite grain aggregates (Fig. 4d-e). The d-spacing measurements,  
197 obtained from the ring-shaped Selected Area Electron Diffraction (SAED) pattern of  
198 ultrafine-grained material, confirm that ultrafine grains are composed of calcite (Fig. 4f). In  
199 particular, rings I and II correspond to  $3.82$  and  $3.00 \text{ \AA}$  spacing (Fig. 4f), in strong agreement  
200 with the  $3.85$  and  $3.03 \text{ \AA}$  of reference calcite (012 and 104 reflections, respectively).

201 When deforming through Stage III, up to  $d = 1.44-1.46$  m (Fig. 1c-d), samples show the  
202 localisation of slip in a cohesive SZ, < 150 mm thick, and the formation of shiny, mirror-like  
203 SS's (Fig. 5a). The bulk slip zone configuration is similar to those seen during Stage II (Fig.  
204 4a-b), but the grain scale textures are very different. Low porosity SS's ( $D \approx 600-700$  nm)  
205 separate thin layers of nanograin ( $D \approx 100-600$  nm) aggregates with markedly polygonal  
206 textures and straight grain boundaries (Fig. 5b-c). SEM images show that the SS's and the  
207 thin layers (tl) are composed of relatively compact, polygonal nanostructures of calcite grains,  
208 with  $120^\circ$  triple junction contacts between equiaxial grains (Fig. 5b-c). Patches of polygonal  
209 nanograins with coarser (600-700 nm, Fig. 5b) and finer ( $\leq 100$  nm, Fig. 5c) grainsize are  
210 observed in the tl, in contrast to the polygonal nanograins on the SS which display a more  
211 uniform, but larger grainsize distribution (600-700 nm) (Fig. 5b-c). TEM analyses show that  
212 the finer and coarser calcite grains in the tl have low dislocation densities, as shown by their  
213 homogeneous TEM contrast, regardless of their crystal orientation (Fig. 5d). Relatively large  
214 cavities (e.g., C in Fig. 5e) occur along grain boundaries or at triple junctions, whereas  
215 smaller rounded bubbles are trapped within calcite grains (Fig. 5e). Calcite clasts from the tl  
216 in the SZ exhibit irregular, lobate crystal boundaries, surrounded by thin (<10 nm) rims of  
217 amorphous material of limited extent (Fig. 5f). Calcite grains do not show crystal preferred  
218 orientation, as they are characterized by ring-shaped SAED patterns (Fig. 5g). Measured d-  
219 spacing confirms that the polygonal grains are calcite (Fig. 5g).

## 220 **4.2 Phase transformation and annealing processes**

221 We found little evidence for phase transformations that might cause weakening in our  
222 experiments. Microstructural and mineralogical observations show that the development of  
223 degassing bubbles (Figs. 4e, 5e) and amorphization rims (Figs. 4e, 5f), indicative of  
224 decarbonation reactions, are limited to the boundaries of calcite grains in the SZ of samples  
225 deformed through Stage II and Stage III. In both cases, SAED pattern analyses revealed that

226 the clasts in the SZ are composed of calcite (Figs. 4f, 5g), confirming that decarbonation  
227 reactions in the SZ of samples deformed up to Stage III were not quantitatively significant.  
228 We interpret this as being due to the kinetics of the decarbonation reaction requiring exposure  
229 to decomposition temperatures for periods much longer than the few fractions of a second that  
230 occurred during our experiments (De Paola et al., 2011a). This interpretation is supported by  
231 further microstructural evidence showing that widespread and pervasive, intragranular  
232 thermal decomposition processes do affect polygonal calcite grains, when high temperatures  
233 are maintained for longer time periods ( $> 2$  s) during high displacement experiments ( $d > 5$  m)  
234 (Supplementary Information 2). Thus we propose that the observed weakening is not caused  
235 by thermally activated phase transitions when fault displacements are  $< 1.5$  m.

236 Microstructural observations on samples deformed up to Stage III show the presence of  
237 localised patches of small ( $\leq 100$  nm) polygonal nanograins in the tl of the SZ. The grainsizes  
238 are similar to those observed in the tl of samples deformed up to Stage II (Figs. 4b-d, 5b-c).  
239 However, slightly larger polygonal nanograins (600-700 nm) have also been observed on both  
240 the SS and in the tl of samples deformed up to Stage III (Fig. 5b-c), suggesting that grain  
241 growth processes occurred in the nanograins of the experimental SZ. Grain growth kinetics  
242 and the grainsize that can be attained by normal grain growth are described by the well know  
243 equation (e.g., Covey-Crump, 1997)

$$244 \quad d^{\frac{1}{n}} - d_0^{\frac{1}{n}} = k_0 t e^{-\frac{H}{RT}} \quad \text{Eq. 2}$$

245 where  $d$  is the grainsize,  $d_0$  is the initial grainsize,  $t$  is the duration of the growth period,  $n$  is a  
246 dimensionless constant which depends on the process controlling the growth rate,  $k_0$  is the  
247 pre-exponential factor,  $H$  is the apparent activation enthalpy of the process controlling the  
248 grain growth,  $R$  is the gas constant and  $T$  is the temperature. During sample deformation up to  
249 Stage II ( $T = 500$  °C) and Stage III ( $T = 800$ - $1000$  °C) (Supplementary Information Table 1),  
250 the maximum temperatures inferred in the slip zone are only attained for a fraction of a

251 second, and it takes  $< 10$  s for our sample to cool down to  $T < 100$  °C. Hence, we assume that  
252  $t = 1$  s is a conservative estimation of the time-scale upon which grain growth, due to static  
253 recrystallization, may occur in the slip zone. The parameters  $n = 0.5$ ,  $k_0 = 3.5502 * 10^{-10} \mu\text{m}^{1/n}$   
254  $\text{s}^{-1}$  (obtained from  $k_{979\text{ °K}} = 5.5626 * 10^{-3} \mu\text{m}^{1/n} \text{s}^{-1}$ ),  $H = 240 * 10^3 \text{ J mol}^{-1}$ ,  $R = 8.3145 \text{ J °K}^{-1}$   
255  $\text{mol}^{-1}$ , obtained by Covey-Crump (1997) for the pore-fluid absent conditions, were used to  
256 solve Eq. 2, and to calculate the maximum theoretical increase in grain size,  $d$ , from an initial  
257 grain size  $d_0 = 0.1 \mu\text{m}$ , when growth time  $t = 0.1, 1, 10$  s and temperature  $T = 500, 800, 900,$   
258  $1000$  °C (Fig. 6). The results show that, for conditions similar to those attained in samples  
259 deformed up to Stage II (e.g.  $T = 500$  °C and initial grain size  $d_0 = 0.1 \mu\text{m}$ ), no grain growth  
260 should occur in our samples (Fig. 6). Under these conditions, the activation of grain boundary  
261 migration processes requires timescales significantly longer than the overall duration and  
262 quenching phase of our experiments (Fig. 6). These results agree well with our  
263 microstructural observations on SS and tl nanograin aggregates showing  $D \leq 100$  nm and a  
264 lack of diagnostic large and dislocation-free grains that would be expected to form during  
265 annealing.

266 For conditions similar to those attained in samples deformed up to Stage III (e.g.  $T = 800-$   
267  $1000$  °C and initial grain size  $d_0 = 0.1 \mu\text{m}$ ), grain growth is predicted to occur for the range of  
268 time  $0.1 \text{ s} \leq t \leq 10 \text{ s}$  considered (Fig. 6). At these conditions, grain boundary migration  
269 processes could be activated within 0.1 s from the attainment of the high temperatures  
270 reached in our experiments when deformed up to Stage III (Fig. 6). Our microstructural  
271 observations of polygonal, nanograin aggregates on the SS and in the tl show grain growth  
272 from initial values of  $d_0 \leq 100$  nm up to  $D = 600-700$  nm, which is lower than the maximum  
273 grainsize  $d = 2.25 \mu\text{m}$  predicted by grain growth calculations at  $T = 1000$  °C and  $t = 1$  s (Fig.  
274 6). TEM analyses show that the polygonal calcite grains do have low dislocation density, but  
275 there is still a lack of diagnostic large and dislocation-free grains, which would be expected to



276 form during complete annealing. We conclude that static recrystallization and growth of the  
277 nanograin aggregates on the SS and within localised patches in the tl may have occurred after  
278 the experiments, during the cooling stage of samples deformed up to Stage III, although the  
279 integration of microstructural and theoretical data show that grain growth may only have  
280 caused a partial annealing of the original fabric. Elements of this fabric may still be preserved  
281 in the tl as patches of fine grainsize polygonal nanograins (see Fig. 5c). The attainment of  
282 high  $T$  for short durations ( $t \leq 1$  s) and the presence of second-phase materials (e.g.,  
283 amorphous decomposed material, Fig. 5f) and pores (e.g., degassing bubbles, Fig. 5e) pinning  
284 the grain boundaries (Olgard and Evans, 1986), may have limited grain growth during our  
285 experiments. This plausibly explains the local preservation of patches of finer polygonal  
286 nanograins and the lower grainsizes observed than those theoretically predicted (Fig. 6).

## 287 **5. Natural faults**

288 In the last decade a series of studies have documented the nucleation and/or propagation of  
289 significant earthquakes through thick sequences of carbonates (e.g. Miller et al., 2004;  
290 Valoroso et al., 2014). Motivated by these observations, several workers have focussed on the  
291 study of carbonate-bearing faults exhumed from the seismogenic crust in order to improve the  
292 characterization of fault zone structure and deformation processes (e.g. De Paola et al., 2008;  
293 Smith et al., 2011; Rowe et al., 2012; Collettini et al., 2013; Siman-Tov et al., 2013; Bullock  
294 et al., 2014). Here as a natural example, we use a large-offset ( $\approx 600$  m) fault exposed in the  
295 seismic belt of the Apennines, Italy. The fault is 10 km long with a maximum width of about  
296 1.5 km and consists of 5 sub-parallel segments (Collettini et al., 2014). At the outcrop scale  
297 the fault structure is characterized by striated and mirrored SS's (Fig. 7a), similar to those  
298 observed in other carbonate-hosted, seismically active faults (Smith et al., 2013, Siman-Tov  
299 et al., 2013). Sampling and microstructural studies across the SS reveal a natural cohesive SZ  
300 ( $<150$   $\mu\text{m}$  thick) characterized by parallel SS's (Fig. 7b, c).

301 SEM investigations of the SZ show calcite grains with lobate and faint grain boundaries.  
302 Grain boundaries are characterized by the concentration of voids and/or vesicles, indicating  
303 limited thermal decomposition of calcite (Fig. 7b and Collettini et al., 2014). TEM analyses  
304 show that some portions of the SS's and the SZ material are made of micrometer-sized calcite  
305 crystals, which commonly show nanoscale polysynthetic twinning. High dislocation densities  
306 and subgrain boundary formation indicate that twin lamellae have experienced intense strain.  
307 The pervasive occurrence of subgrain boundaries along twinning planes suggests that  
308 twinning predates the development of dislocations, dislocation walls and calcite nanograins  
309 ( $D = 200\text{-}300\text{ nm}$ ). Other portions of the SS's and SZ material show calcite nanograin ( $D \leq$   
310  $100\text{ nm}$ ) aggregates with a polygonal texture; the nanograins have straight grain boundaries  
311 with  $120^\circ$  triple junction contacts between equiaxial grains, and display no preferred  
312 elongation (Fig. 7d). These natural microstructures are strikingly similar to those observed in  
313 the experimentally deformed samples during Stage III (Fig. 5c).

## 314 **6. Discussion**

### 315 **6.1 Micro-scale deformation mechanisms during earthquake propagation**

316 In the experimental samples, a localised slip zone, up to  $150\text{ }\mu\text{m}$  thick, develops in the  
317 early stages of deformation (Stage I) when the SZ material is poorly consolidated, bounded by  
318 slip surfaces, and made of fine-grained, angular clasts ( $1 \leq D \leq 5\text{ }\mu\text{m}$ ). Brittle fracturing and  
319 cataclasis are the dominant deformation mechanisms observed in samples deformed up to  
320 Stage I, at relatively low temperatures ( $\leq 100\text{ }^\circ\text{C}$ ), and it is these mechanisms that likely  
321 control shear localisation and grain size reduction in the slip zone (Fig. 3) (Bullock et al.,  
322 2015; Smith et al., 2015). In our experiments — unlike those of Verberne et al. (2014) — we  
323 do not observe the development of shiny, mirror-like slip surfaces and of nanoscale materials  
324 in the SZ of samples deformed up to Stage I (up to  $7\text{ mm}$  slip). Sliding friction values

325 predicted by Byerlee's rule (Byerlee, 1978) match those measured during experiments  
326 arrested in Stage I (Fig. 1).

327 SEM analyses of samples deformed up to Stage II show that the SZ material becomes  
328 cohesive and contains multiple SS's, which sandwich thin ( $\approx 5 \mu\text{m}$ ) porous layers of sub-  
329 rounded nanograins (Fig. 4). TEM analyses show larger clasts of calcite ( $D \approx 1 \mu\text{m}$ ) dispersed  
330 within a porous assemblage of calcite nanograins,  $\leq 100 \text{ nm}$  in size. These larger calcite clasts  
331 exhibit a high density of free dislocations and host subgrains ( $D \leq 100 \text{ nm}$ ) (Fig. 4d-e). As  
332 temperatures rise during Stage II, due to frictional heating ( $T \approx 550 \text{ }^\circ\text{C}$ ), intracrystalline  
333 plasticity mechanisms, active at  $T \leq 600 \text{ }^\circ\text{C}$ , start to accommodate intragranular strain and the  
334 development of nanoscale subgrains ( $D \leq 100 \text{ nm}$ ) in the thin layers of the slip zone (Fig. 4d-  
335 e).

336 When deformation progresses through Stage III, samples show a bulk slip-zone  
337 configuration similar to Stage II, but the grain-scale microstructures are very different. SEM  
338 and TEM analyses of thin layers of nanograin ( $D \approx 100\text{-}600 \text{ nm}$ ) aggregates between the SS's  
339 exhibit polygonal grain boundaries, showing  $120^\circ$  triple junctions between equiaxial grains  
340 (Fig. 5b-e). The grains display no preferred elongation, no crystal preferred orientation (based  
341 on SAED measurements) and low dislocation densities (Fig. 5d-g), possibly due to high  
342 temperature ( $\geq 900 \text{ }^\circ\text{C}$ ) GBS deformation mechanisms. The observed micro-textures in  
343 experimental (Fig. 8a) and natural slip zones (Fig. 8b) are strikingly similar to those predicted  
344 by theoretical studies (Fig. 8c, Ashby and Verrall, 1973), and those observed during  
345 experiments on metals (Chandra, 2002) and fine-grained carbonates (Walker et al., 1990,  
346 Schmid et al., 1977), at temperatures  $\leq 1000 \text{ }^\circ\text{C}$ , where superplastic behaviour due to  
347 grain-size-sensitive GBS has been inferred. Hence, we propose that the preservation of  
348 equiaxial polygonal nano-grains ( $D \leq 100 \text{ nm}$ ), with low dislocation densities, is diagnostic of  
349 GBS mechanisms associated with superplastic behaviour (Verberne et al., 2013, 2014).

350 Our SEM and TEM observations show that the synthetic carbonate gouges deformed up to  
351 Stage III in our experiments preserve microstructural evidence for the operation of GBS  
352 accommodated by *both* diffusion and dislocation creep (Fig. 5c-e). The polygonal nanograins  
353 developed during Stage III are characterized by a much lower dislocation density compared to  
354 those observed during Stage II. This may be due to the establishment of less favourable  
355 conditions for the operation of dislocation creep (i.e., high  $T$ , small grain size) attained at the  
356 transition from Stage II to Stage III in our experiments. Despite microstructural evidence for  
357 the simultaneous occurrence and operation of both diffusion- and dislocation-dominated GBS,  
358 more microstructural work is needed to quantify their relative contribution to the deformation  
359 of nanoscale materials at high strain rates and temperatures. Overall, the distinctive textures  
360 observed indicate a switch from low-temperature plasticity and cataclasis (Stages I, II) to  
361 GBS mechanisms (Stage III).

362 Finally, we suggest that the re-strengthening observed during deceleration at the end of the  
363 friction experiments (Stage IV, Fig. 1c-d) results from a decrease in the activity of slip zone-  
364 localised GBS associated with decreasing temperatures.

## 365 **6.2 Slip zone strength: can grain size sensitive creep control fault strength during** 366 **earthquake propagation?**

367 Our experimental results and microstructural observations reveal evidence for the  
368 operation of both intracrystalline plasticity and GBS-accommodated flow processes in slip  
369 zones deformed at earthquake velocities. The evolution of distinctive micro-textures observed  
370 in the slip zone suggests that the transition from low-temperature plasticity and cataclasis ( $T \leq$   
371  $500\text{ }^{\circ}\text{C}$  during Stages I and II, Figs. 2-4) to GBS-accommodated flow ( $T \geq 800\text{ }^{\circ}\text{C}$  during  
372 Stage III, Figs. 2,5,8) coincides with the onset of the weakening measured in the tested  
373 materials at seismic conditions (Figs. 1-2). Verberne et al. (2014) were the first to speculate  
374 that GBS-accommodated flow could occur at high strain rates and temperatures during

375 rupture propagation in carbonate rocks. Green et al. (2015) produced further experimental  
376 evidence for the occurrence of phase transformation and GBS-accommodated flow in  
377 carbonate rocks shearing at seismic slip rates and temperatures, and proposed that these  
378 mechanisms could be associated with the onset of dynamic weakening in carbonate rocks. In  
379 our experiments, phase transformations, such as decarbonation of calcite, that might lead to  
380 weakening are of limited extent. Hence, whilst we agree with the previous hypotheses that  
381 GBS-accommodated flow can weaken faults at seismic slip rates (Green et al., 2015;  
382 Verberne et al., 2014), we suggest that the onset of the observed weakening does not require  
383 thermally-activated phase transitions to occur in carbonate rocks.

384 We now calculate flow stresses to add new evidence to the hypothesis that GBS-  
385 accommodated flow can weaken faults at high strain rates and temperatures, prior to the onset  
386 of phase transformations, and thus control earthquake propagation in the shallow crust. We  
387 use published constitutive flow laws for both dislocation creep and diffusion-dominated GBS  
388 in carbonates at temperatures  $\geq 500$  °C (Ashby and Verral, 1973; Schmid et al., 1977; Walker  
389 et al. 1990), applying a range of strain rates and grain sizes representative of our experimental  
390 conditions (Supplementary Information Table I).

### 391 **6.2.1 Flow laws and state variables**

392 The predicted flow stress for end-member type deformation mechanisms, dislocation creep  
393 and diffusion creep, can be modelled by the constitutive flow law

$$394 \quad \dot{\gamma} = A^* D^{-b} e^{-\frac{H}{RT}} \tau^n \quad \text{Eq. 3}$$

395 where  $\dot{\gamma}$  is the shear strain rate,  $A^*$  is a pre-exponential factor,  $H$  is the apparent activation  
396 energy for creep,  $R$  is the gas constant,  $T$  is the absolute temperature,  $\tau$  is the shear stress,  $n$   
397 the stress exponent,  $D$  is the grain size and  $b$  is the grain size exponent. For dislocation creep,  
398  $b$  is 0 and  $3 < n < 7$ , whereas for diffusion creep (which must include GBS)  $2 < b < 3$  and  $n =$   
399 1. For dislocation-accommodated GBS,  $b$  and  $n$  lie somewhere between these two end

400 members, so that  $1 < n < 3$  values are predicted for grainsize-sensitive creep regimes (Ashby  
401 and Verral, 1973), when the superposition of the two end-member mechanisms  
402 accommodates viscous flow (Ashby and Verral, 1973; Schmidt et al., 1977). In the latter case  
403 ( $1 < n < 3$ ), the overall creep rate should be given, to a sufficient approximation, by their  
404 relative contribution (Ashby and Verral, 1973).

405 The parameters  $b = 0$ ,  $n = 4.70$ ,  $A = 0.046$  ( $\text{s}^{-1} \text{bar}^{-n}$ ),  $H = 71$  ( $\text{kcal mole}^{-1}$ ),  $R = 1.987 \cdot 10^{-3}$   
406 ( $\text{kcal } ^\circ\text{K mole}^{-1}$ ), and  $b = 3$ ,  $n = 1.7$ ,  $A^* = 9.55 \cdot 10^4$  ( $\text{s}^{-1} \text{bar}^{-n}$ ),  $H = 51$  ( $\text{kcal mole}^{-1}$ ),  $R =$   
407  $1.987 \cdot 10^{-3}$  ( $\text{kcal } ^\circ\text{K mole}^{-1}$ ), obtained for deformed calcite aggregates from Schmid et al.  
408 (1977), were used to solve Eq. 3 and to calculate the flow stress  $t$  predicted for dislocation  
409 creep and grainsize-sensitive GBS-accommodated flow, respectively, when  $T = 600, 1000$   $^\circ\text{C}$   
410 and  $\dot{\gamma} = 1 - 3 \cdot 10^3$   $\text{s}^{-1}$  (Fig. 9).

411 The average shear strain,  $\gamma$ , values have been calculated by  $\gamma = \tan \phi = r\theta/2h$ , where  $\phi$  is the  
412 angular shear,  $r$  is the outer diameter of the sample,  $\theta$  is the angular displacement in radians  
413 and  $h$  is the average slip zone thickness. Shear strain rate,  $\dot{\gamma}$ , can then be calculated as the  
414 ratio  $\dot{\gamma} = \Delta\gamma/\Delta t$ , where  $\Delta t$  is the duration of each experiment from the onset of a specific  
415 deformation mechanism. An average value,  $h = 150$   $\mu\text{m}$ , has been assumed during shear strain  
416 calculations, based on optical and scanning electron microscope images, which show the  
417 development of a slip zone, due to shear localisation, from the very early stages of  
418 deformation when  $d$  is only a few mm (Fig. 3a). Strain rate values calculated for each  
419 deformation mechanism observed during the different stages of the experiments have been  
420 used as reference values during the flow stress calculations (Fig. 9, Table I). The grain size  
421 range  $D = 10\text{-}600$  nm was used during flow stress calculation of grainsize-sensitive GBS-  
422 accommodated flow, based on microstructural observations of the slip zone material produced  
423 during Stage II and Stage III deformation (Figs. 4-5).

## 424 **6.2.2 Flow stress values and interpretation of results**

425 Flow stress calculations, performed using Eq. 3, show that dislocation creep mechanisms  
426 operate at higher flow stress values ( $\tau > 100$  MPa) than grain size-sensitive GBS in the range  
427 of temperatures ( $T = 600$ - $1000$  °C) and strain rates ( $\dot{\gamma} = 1$ - $3 \times 10^3$  s<sup>-1</sup>) considered, when grain  
428 size  $D < 600$  nm (Fig. 9). For a given temperature, the flow stress increases with strain rate at  
429 a steeper gradient during GBS than during dislocation creep (Fig. 9). For a given temperature  
430 and a fixed strain rate, the flow stress due to GBS decreases with grain size (Fig. 9). At  $T =$   
431  $600$  °C and high strain rates ( $\dot{\gamma} \geq 1000$  s<sup>-1</sup>), the two mechanisms would operate at similar, very  
432 high flow stress values ( $\tau \approx 3000$  MPa) for a grain size of about  $100$  nm (Fig. 9a). Under these  
433 conditions, the calculated flow stress values are always significantly higher than the values  
434 measured during our laboratory experiments (Fig. 9a). At  $T = 1000$  °C and high strain rates ( $\dot{\gamma}$   
435  $\geq 1000$  s<sup>-1</sup>), grain size-sensitive GBS flow would operate at much lower flow stress values ( $\tau \leq$   
436  $12$  MPa) than dislocation creep ( $\tau \approx 100$  MPa), for grain size  $D \leq 100$  nm (Fig. 9b). Under  
437 these conditions, the shear stress values measured during our laboratory experiments are  
438 between the calculated flow stress values for grain size  $10 < D < 100$  nm (Fig. 9b).

439 Our microstructural observations suggest that brittle fracturing and cataclasis are the  
440 mechanisms that control shear localisation and grain size reduction in the slip zone at  
441 relatively low temperatures ( $\leq 100$  °C). Stress levels predicted by Byerlee's sliding friction  
442 values (Byerlee, 1978) match those measured during Stage I (Fig. 10). Very little is known  
443 about how grain size reduction to submicron levels actually occurs under the conditions  
444 attained during our experiments ( $T \geq 500$  °C), where samples have been deformed up to Stage  
445 II (Green et al., 2015; Verberne et al., 2013, 2014). Here, we propose that, as temperatures  
446 rise during Stage II, due to frictional heating ( $\geq 500$  °C), dislocation creep mechanisms start  
447 to accommodate intragranular strain and play a key role in producing nanoscale subgrains  
448 ( $D \leq 100$  nm) in the slip zone (Fig. 4). Note that during Stage II, nanoparticles are present in  
449 the slip zone and seismic slip rates have been attained. However, the measured frictional

450 strength of the experimental faults still lies within Byerlee's range of values  $\mu = 0.68 - 0.80$   
451 (Fig. 1, Supplementary Information Table I). In the absence of microstructural evidence for  
452 the operation of pressure solution or diffusion creep (e.g., Verberne et al., 2014), it is  
453 suggested that the slip zone bulk strength at this stage is still controlled by cataclastic  
454 frictional sliding rather than by dislocation creep or nanopowder lubrication mechanisms.  
455 This is in accord with our flow stress calculations, which predict flow stresses for dislocation  
456 creep that are up to about 3 orders of magnitude higher than the measured ones at  $T = 600\text{ }^{\circ}\text{C}$   
457 and  $\dot{\gamma} \geq 1 \cdot 10^2\text{ s}^{-1}$  (Figs. 9a, 10). When  $T \approx 1000\text{ }^{\circ}\text{C}$  and  $\dot{\gamma} \approx 3 \cdot 10^3\text{ s}^{-1}$  are attained during Stage  
458 III, micro-textures diagnostic of both dislocation creep and grain-size-sensitive GBS are  
459 observed, the latter becoming widespread within the slip zone (Fig. 5). Under these  
460 temperature and strain rate conditions, the flow stresses predicted for grain-size-sensitive  
461 GBS-accommodated flow, for grain size  $D < 100\text{ nm}$  observed in the slip zone at the onset of  
462 weakening, are lower than those predicted by Byerlee's friction and, within the same order of  
463 magnitude as the values measured during the experiments (Fig. 10).

464 Our microstructural observations are similar to those of previous studies showing that,  
465 under certain conditions, fine-grained geological materials deform by diffusion-  
466 accommodated GBS and dislocation-accommodated GBS (Schmid et al., 1977; Walker et al.,  
467 1990). This combination of mechanisms appears to be capable of explaining not only the  
468 observed relation between strain rate and stress (Schmid et al., 1977; Walker et al., 1990;  
469 Hirth and Kohlstedt, 2003; Mecklenburgh et al., 2010; Goldsby and Kohlstedt, 2001), but also  
470 most of the microstructural and topological features of materials displaying superplastic  
471 behaviour (Ashby and Verrall, 1973; Schmid et al., 1977; Walker et al., 1990; Hirth and  
472 Kohlstedt, 2003; Mecklenburgh et al., 2010; Goldsby and Kohlstedt, 2001; Verberne et al.,  
473 2015; Green et al., 2015).



474 We propose therefore that the activation of grainsize-sensitive GBS deformation  
475 mechanisms in the nanograin aggregates ( $D < 100$  nm) of the localised slip zone, at high  
476 temperatures ( $T \approx 1000$  °C) and strain rates  $\dot{\gamma} \geq 1000$  s<sup>-1</sup>, controls the onset of dynamic  
477 weakening of carbonate faults at seismic slip rates (Fig. 10). Note, however, that the cataclasis  
478 and intragranular dislocation creep operating during the earlier stages of slip are critical,  
479 precursory processes needed to produce the nanoscale grain sizes required to activate  
480 grainsize-sensitive creep mechanisms. Finally, the re-strengthening observed during the  
481 decelerating phase of deformation can be explained by the falling temperature “switching off”  
482 slip zone-localised GBS flow, leading to a return to frictional sliding.

### 483 **6.2.3 Limitations and approximation of flow stress calculations and interpretations**

484 The calculated flow stress values have been obtained by extrapolating published  
485 constitutive flow laws for grainsize-sensitive GBS in carbonates to the conditions attained  
486 during our experiments (Fig. 9, Tables I). The flow stress values obtained for the  
487 temperatures, strain rates and grain sizes attained during our experiments, at the onset of  
488 weakening, are within about one order of magnitude of those measured during our  
489 experiments (Figs. 9-10). The remaining discrepancies are likely due to the approximation of  
490 the estimated slip zone parameters (e.g., grain size and SZ thickness), the experimental  
491 conditions ( $\dot{\gamma}$ ), and the simplistic extrapolation of existing flow laws to smaller, sub-micron  
492 grain sizes and to strain rates which are a few orders of magnitude higher than those at which  
493 they were obtained.

494 In our study we provide evidence that the onset of weakening during shearing at high  
495 velocity coincides with the activation of thermally-induced deformation mechanisms (e.g.,  
496 grainsize-sensitive GBS) within thin layers of nanograins sandwiched by slip surfaces. To a  
497 first approximation, the measured drop in strength is in agreement with our flow stress  
498 calculations, suggesting that strain could be accommodated more efficiently by these

499 mechanisms within the weaker thin layers than by frictional sliding along the SS (Fig. 5b-c).  
500 A quantitative estimation of the strain partitioning between sliding along the SS and  
501 deformation within the thin layers will allow the conceptual model described above to be  
502 proven, and provide more constrained strain rate values to be applied in the flow stress  
503 calculations. At the present stage, these tasks still present some significant practical  
504 challenges in rotary shear apparatus experiments and advanced microstructural studies on the  
505 deformed materials.

## 506 **7. Conclusions**

507 Our observations of experimentally and naturally produced carbonate faults suggest that  
508 grainsize-sensitive GBS deformation mechanisms can operate in geological materials  
509 deformed at high strain rates along frictionally heated seismogenic slip surfaces at the onset  
510 of dynamic weakening after a few centimetres of slip ( $d > 10$  cm), before the occurrence of  
511 bulk phase transformations. The observed microstructures are similar to those seen at low and  
512 high strain rates in carbonates (Verberne et al., 2014; Green et al., 2015), and at high strain  
513 rates for a range of nano-phase alloys and ceramics in association with superplastic behaviour,  
514 where grainsize-sensitive creep regimes develop due to the combined operation of  
515 dislocation/diffusion creep. Our findings provide a plausible explanation for both the low  
516 flow stresses measured at seismic slip rates in carbonate rocks, and most of the  
517 microstructural and topological features of the deformed materials. A regime of frictionally-  
518 induced grainsize-sensitive GBS can thus account for the self-lubrication and dynamic  
519 weakening of carbonate faults during earthquake propagation in nature.

## 520 **Acknowledgements**

521 This study was supported by the Natural Environment Research Council (NERC Standard  
522 Grant NE/H021744/1 awarded to NDP and REH), and the ERC Starting Grant GLASS no.  
523 (259256). L. Bowen (G.J. Russell Microscopy Facility, Durham University, UK) provided

524 invaluable assistance during SEM and TEM analyses. J. Mecklenburgh, L. Hansen and C.  
525 Spiers are thanked for providing helpful comments improving the quality of the text and of  
526 our interpretations.

## 527 **References**

528 Ashby, M.F., Verrall, R.A., 1973. Diffusion-Accommodated Flow and Superplasticity. *Acta*  
529 *Metallurgica* 21, 149-163.

530 Ashby, M.F.a.V., R.A., 1977. Micromechanics of flow and fracture, and their relevance to the  
531 rheology of the upper mantle. *Philosophical Transactions of the Royal Society of London*  
532 288, 59-95.

533 Bullock, R.J., De Paola, N., Holdsworth, R.E., Trabucho-Alexandre, J., 2014. Lithological  
534 controls on the deformation mechanisms operating within carbonate-hosted faults during the  
535 seismic cycle. *J. Struct. Geol.* 58, 22-42.

536 Bullock, R.J., De Paola, N. & Holdsworth, R.E., 2015. An experimental investigation into the  
537 role of phyllosilicate content on earthquake propagation during seismic slip in carbonate  
538 faults. *Journal of Geophysical Research: Solid Earth* 120(5), 3187-3207.

539 Boullier, A.M., Gueguen, Y., 1975. Sp-Mylonites - Origin of Some Mylonites by Superplastic  
540 Flow. *Contrib Mineral Petr* 50, 93-104.

541 Byerlee, J., 1978. Friction of Rocks. *Pure Appl Geophys* 116, 615-626.

542 Chandra, N., 2002. Constitutive behavior of superplastic materials. *International Journal of*  
543 *Non-Linear Mechanics* 37, 461-484.

544 Collettini, C., Viti, C., Tesei, T., Mollo, S., 2013. Thermal decomposition along natural faults  
545 during earthquakes. *Geology* 41, 927e930. <http://dx.doi.org/10.1130/G34421.1>.

546 Collettini, C., Carpenter, B.M., Viti, C., Cruciani, F., Mollto, S., Tesei, T., Trippetta, F.,

547 Valoroso, L., Chiaraluce, L., 2014. Fault structure and slip localization in carbonate bearing

548 normal faults: an example from the Northern Apennines of Italy. *J. Struct. Geol.* 67, 154–166.  
549 <http://dx.doi.org/10.1016/j.jsg.2014.07.017>.

550 Covey-Crump, S.J., 1997. The normal grain growth behaviour of nominally pure calcitic  
551 aggregates. *Contribution to Mineralogy and Petrology* 129, 239-254.

552 De Paola, N., Collettini, C., Faulkner, D.R., Trippetta, F., 2008. Fault zone architecture and  
553 deformation processes within evaporitic rocks in the upper crust. *Tectonics* 27.  
554 <http://dx.doi.org/10.1029/2007TC002230>.

555 De Paola, N., Chiodini, G., Hirose, T., Cardellini, C., Caliro, S. & Shimamoto, T., 2011a. The  
556 geochemical signature caused by earthquake propagation in carbonate-hosted faults. *Earth  
557 and Planetary Science Letters* 310(3-4), 225-232.

558 De Paola, N., Hirose, T., Mitchell, T., Di Toro, G., Viti, C., Shimamoto, T., 2011b. Fault  
559 lubrication and earthquake propagation in thermally unstable rocks. *Geology* 39, 35-38.

560 De Paola, N., 2013. Nano-powder coating can make fault surfaces smooth and shiny:  
561 implications for fault mechanics? *Geology* 41, 719-720.

562 Di Toro, G., Han, R., Hirose, T., De Paola, N., Nielsen, S., Mizoguchi, K., Ferri, F., Cocco,  
563 M., Shimamoto, T., 2011. Fault lubrication during earthquakes. *Nature* 471, 494-+.

564 Fondriest, M., Smith, S.A.F., Candela, T., Nielsen, S.B., Mair, K., Di Toro, G., 2013. Mirror-  
565 like faults and power dissipation during earthquakes. *Geology* 41, 1175-1178.

566 Goldsby, D. L., Kohlstedt, D. L., 2001. Superplastic deformation of ice: Experimental  
567 observations. *J Geophys Res-Sol Ea* 106, 11017-11030.

568 Goldsby, D.L., Tullis, T.E., 2011. Flash Heating Leads to Low Frictional Strength of Crustal  
569 Rocks at Earthquake Slip Rates. *Science* 334, 216-218.

570 Green, H.W., Shi, F., Bozhilov, K., Xia, G., Reches, Z., 2015. Phase Transformation and  
571 Nanometric Flow Cause Extreme Weakening During Faulting. *Nature Geoscience* DOI:  
572 10.1038/NGEO2436.

573 Han, R., Hirose, T., Shimamoto, T., 2010. Strong velocity weakening and powder lubrication  
574 of simulated carbonate faults at seismic slip rates. *J Geophys Res-Sol Ea* 115, -.

575 Hiraga, T., Miyazaki, T., Tasaka, M., Yoshida, H., 2010. Mantle superplasticity and its self-  
576 made demise. *Nature* 468, 1091-U1490.

577 Hirose, T., Shimamoto, T., 2005. Growth of molten zone as a mechanism of slip weakening  
578 of simulated faults in gabbro during frictional melting. *J Geophys Res-Sol Ea* 110, -.

579 Hirth, G., and D. L. Kohlstedt, 2003. Inside the subduction factory edited by J. Eiler, pp. 83-  
580 105, American Geophysical Union, Washington D. C.

581 Kohlstedt, D.L., Evans, B., Mackwell, S.J., 1995. Strength of the Lithosphere - Constraints  
582 Imposed by Laboratory Experiments. *J Geophys Res-Sol Ea* 100, 17587-17602.

583 Lankford, J., 1996. High strain rate compression and plastic flow of ceramics. *Journal of*  
584 *Materials Science Letters* 15, 745-750.

585 Mecklenburgh, J., Heidelbach, F., Mariani, E., Mackwell, S. and Seifert, F., 2010. Rheology  
586 and microstructure of (Ca<sub>0.9</sub>,Sr<sub>0.1</sub>)TiO<sub>3</sub> perovskite deformed in compression and torsion. *J*  
587 *Geophys Res-Sol Ea* 115.

588 Olgaard, D. L., Evans, B., 1986. Effect of second-phase particles on grain growth in calcite.  
589 *Contribution to Mineralogy and Petrology*, 69, C272-C277.

590 Passchier, C.W.a.T., R.A.J., 2005. *Micro-tectonics*. Springer, 1-365.

591 Poirier, J.P., 1985. *Creep of Crystals*. Cambridge Earth Sciences Series, 1-258.

592 Reches, Z., Lockner, D.A., 2010. Fault weakening and earthquake instability by powder  
593 lubrication. *Nature* 467, 452-U102.

594 Ree, J.H., Ando, J.I., Han, R., Shimamoto, T., 2014. Coseismic microstructures of  
595 experimental fault zones in Carrara marble. *J Struct Geol* 66, 75-83.

596 Rice, J.R., 2006. Heating and weakening of faults during earthquake slip. *J Geophys Res-Sol*  
597 *Ea* 111, -.

598 Rowe, C.D., Fagereng, A., Miller, J.A., and Mapani, B., 2012. Signature of coseismic  
599 decarbonation in dolomitic fault rocks of the Naukluft Thrust, Namibia. *Earth and Planetary*  
600 *Science Letters* 333, 200–210. doi:10.1016/j.epsl .2012.04.030.

601 Rutter, E.H., 1995. Experimental study of the influence of stress, temperature, and strain on  
602 the dynamic recrystallization of Carrara marble. *J Geophys Res-Sol Ea* 100, 24651-24663.

603 Rutter, E.H., 1999. On the relationship between the formation of shear zones and the form of  
604 the flow law for rocks undergoing dynamic recrystallization. *Tectonophysics* 303, 147-158.

605 Rutter, E.H., Brodie, K.H., 1988. The Role of Tectonic Grain-Size Reduction in the  
606 Rheological Stratification of the Lithosphere. *Geol Rundsch* 77, 295-307.

607 Rutter, E.H., Casey, M., Burlini, L., 1994. Preferred Crystallographic Orientation  
608 Development during the Plastic and Superplastic Flow of Calcite Rocks. *J Struct Geol* 16,  
609 1431-1446.

610 Schmid, S.M., Boland, J.N., Paterson, M.S., 1977. Superplastic Flow in Finegrained  
611 Limestone. *Tectonophysics* 43, 257-291.

612 Scholz, C.H., 1998. Earthquakes and friction laws. *Nature* 391, 37-42.

613 Schubnel, A., Brunet, F., Hilairet, N., Gasc, J., Wang, Y.B., Green, H.W., 2013. Deep-Focus  
614 Earthquake Analogs Recorded at High Pressure and Temperature in the Laboratory. *Science*  
615 341, 1377-1380.

616 Sibson, R.H., 1977. Fault rocks and fault mechanisms. *J Geol Soc London* 133, 191-213.

617 Siman-Tov, S., Aharonov, E., Sagy, A., Emmanuel, S., 2013. Nanograins form carbonate  
618 fault mirrors. *Geology* 41, 703-706.

619 Smith, S.A.F., Billi, A., Di Toro, G., Spiess, R., 2011. Principal slip zones in limestone:  
620 microstructural characterization and implications for the seismic cycle (Tre Monti Fault,  
621 Central Apennines, Italy). *Pure Appl. Geophys.* 168, 2365e2393.

622 <http://dx.doi.org/10.1007/s00024-011-0267-5>.

623 Smith, S.A.F., Di Toro, G., Kim, S., Ree, J.H., Nielsen, S., Billi, A., Spiess, R., 2013.  
624 Coseismic recrystallization during shallow earthquake slip. *Geology* 41, 63-66.  
625 Smith, S.A.F., Nielsen, S., Di Toro, G., 2015. Strain localization and the onset of dynamic  
626 weakening in calcite fault gouge. *Earth Planet. Sc. Lett.* 413, 25-36.  
627 Tisato, N., Di Toro, G., De Rossi, N., Quaresimin, M., Candela, T., 2012. Experimental  
628 investigation of flash weakening in limestone. *J Struct Geol* 38, 183-199.  
629 Valoroso, L., Chiaraluce, L., Collettini, C., 2014. Earthquakes and fault zone structure.  
630 *Geology* 42, 343-346.  
631 Verberne, B.A., Plümper, O., Matthijs de Winter, D.A. and Spiers, C.J., 2014. Superplastic  
632 nanofibrous slip zones control seismogenic fault friction. *Science* 346, ISSUE 6215.  
633 Verberne, B. A., De Bresser, J. H. P., Niemeijer, A. R., Spiers, C. J., De Winter, D. A. M.,  
634 and Plumper, O., 2013. Nanocrystalline slip zones in calcite fault gouge show  
635 intense crystallographic preferred orientation: Crystal plasticity at sub-seismic slip rates at 18  
636 – 150 C. *Geology* 41, 863–866.  
637 Walker, A.N., Rutter, E.H., Brodie, K.H., 1990. Experimental-Study of Grain-Size Sensitive  
638 Flow of Synthetic, Hot-Pressed Calcite Rocks. *Deformation Mechanisms, Rheology and*  
639 *Tectonics* 54, 259-284.

640 **Figure Captions:**

641 **Figure 1 – Experimental data.** a-b) Slip rate vs. displacement data for a set of displacement-  
642 controlled experiments performed at  $\sigma_n = 12, 18$  MPa, and arrested before, during and after  
643 the attainment of target speed,  $v = 1 \text{ ms}^{-1}$ . c-d) Friction coefficient vs. displacement data  
644 showing the evolution of friction during acceleration (Stages I-II), steady-state sliding (Stage  
645 III) and instantaneous deceleration to arrest (Stage IV) of the sample. The inset shows a blow-  
646 up of the data in the main graph.

647 **Figure 2 – Temperature vs. friction coefficient data.** Temperatures calculated for localised,  
648 thin ( $< 150 \mu\text{m}$ ) slip zones plotted vs. the friction coefficient measured during laboratory  
649 experiments performed at seismic, target slip rates ( $1 \text{ ms}^{-1}$ ) on carbonate gouges (Table I).

650 **Figure 3: Microstructural observations of experimental slip zones (Stage I).** a) Scanning  
651 electron microscope (SEM) image showing in plan view the development of a rough SS, due  
652 to the presence of grooves (g) and ridges (r), oriented parallel to the slip direction. b) Optical  
653 microscope image showing in cross-section the formation of a continuous, immature slip zone  
654 (SZ) with variable thickness ( $20\text{-}200 \mu\text{m}$ ), bounded on the upper part by a rough SS. c) SEM  
655 image in plan view showing a magnified, smooth portion of the SS made of fine-grained  
656 clasts ( $1 < D < 5 \mu\text{m}$ ), which are sharply truncated against the SS.

657 **Figure 4 – Microstructural observations of experimental slip zones (Stage II).** a-c)  
658 Optical microscope (a, cross section view) and SEM (b-c, plan view) images show the  
659 development a cohesive slip zone (SZ), and striated slip surface (SS) sandwiching thin layers  
660 made of nanograin aggregates ( $D \leq 100 \text{ nm}$ ) with sub-rounded shape. d) TEM image showing  
661 calcite nanograins ( $\leq 100 \text{ nm}$ ) in contact with a calcite clast (CC) hosting dislocations and  
662 dislocation walls (DW) separating subgrains (SG) ( $D \leq 100 \text{ nm}$ ). e) Calcite clasts (CC)  
663 exhibit “damaged” rims, hosting rounded bubbles and lobate, low-contrast features (arrows)  
664 (Bright-field TEM images). d) Measured d-spacings from ring-shaped SAED pattern confirm  
665 that ultrafine grains are formed by calcite.

666 **Figure 5 – Microstructural observations of experimental slip zones (Stage III).** a-c)  
667 Optical microscope (a, cross section and inset oblique plan views) and SEM (b-c, plan view)  
668 images show the development of a cohesive slip zone (SZ) composed of stacked striated slip  
669 surfaces (SS), sandwiching thin layers (tl) of nanoscale grains. d) TEM images show that tl  
670 are associated with compact polygonal nanostructures of calcite grains, displaying low free  
671 dislocation densities. e) TEM image of relatively large cavities (C) formed along grain



672 boundaries or at triple junctions, whereas smaller rounded bubbles are trapped within calcite  
673 grains (B). f) Calcite clast relic from the thin porous layers in the slip zone (see main text),  
674 exhibiting irregular, lobate crystal boundaries, surrounded by a 10 nm thick amorphous rim  
675 (am). g) Measured d-spacings from single-crystal SAED pattern of polygonal grains from the  
676 thin layers confirm that polygonal grains are formed by calcite (arrows show the  
677 corresponding reciprocal axes).

678 **Figure 6 – Modelled grainsize vs. time during static crystallization.** The graph shows the  
679 maximum, theoretical increase in grain size, obtained by solving Eq. 2 in the main text for  
680 range of temperatures, initial grain sizes and timescales representative of those attained during  
681 sample deformation up to Stage II ( $T = 500\text{ }^{\circ}\text{C}$ ) and Stage III ( $T = 800 - 1000\text{ }^{\circ}\text{C}$ ). The blue  
682 (Stage II) and black (Stage III) rectangles show the range of grainsizes observed in the  
683 experimental slip zones.

684 **Figure 7 – Mesoscale and microstructural observations from natural slip zones.** a)  
685 Outcrop photograph of the M. Maggio fault plane, located in the Apennines of Italy (details in  
686 Collettini et al., 2014), showing its naturally polished, reflective glossy surface. b) Rock  
687 sample cross section including hanging-wall, HW, and footwall, FW, blocks together with the  
688 principal slipping zone (indicated by the arrow) where we performed the microstructural  
689 studies. c) BSE-SEM image in cross section showing that the principal slipping zone is about  
690 100 mm thick (dashed yellow line) and, here, the slip is accommodated along sub-parallel SSs  
691 indicated by yellow arrows. d) Nanostructure composed of polygonal calcite grains in close  
692 association with strain-free calcite crystals.

693 **Figure 8 – Microstructures diagnostic of superplastic behavior: theory vs.**  
694 **experimental/natural slip zone samples.** a-b) SEM images of experimental (a) and natural  
695 (b) slip zones made of compact calcite nanograin aggregates with a polygonal texture,  
696 diagnostic of grainsize sensitive grain boundary sliding (GBS) mechanisms. c) Diagnostic

697 microstructures predicted by superplastic flow accommodated by grain size sensitive GBS,  
698 showing different stages (I-III) of the neighbour switching process (after Ashby and Verrall,  
699 1973).

700 **Figure 9 – Measured and predicted flow stresses.** a-b) Calculated flow stresses for  
701 dislocation creep and grain size sensitive GBS creep (Eq. 2 in the main text) are plotted vs.  
702 strain rates for a range of grain sizes (GBS only) and temperatures, representative of the  
703 conditions attained during sample deformation up to Stage II (a) and Stage III (b). The green  
704 dots represent the measured shear stress attained in our experiments at steady state during  
705 deformation up to Stage III.

706 **Figure 10 – Fault strength evolution with increasing temperatures at high strain rates.**  
707 Shear stresses predicted by frictional sliding (Byerlee, 1978) match those measured during  
708 laboratory experiments at seismic slip rates during Stages I-II (temperature  $\leq 600$  °C). Flow  
709 stress values predicted by a regime of grain size-sensitive GBS creep (Eq. 2 constitutive law in  
710 the main text) at temperatures  $\geq 600$  °C, strain rates =  $3 \cdot 10^3$  s<sup>-1</sup> and grain size  $D < 100$  nm,  
711 observed in the slip zone at the onset of weakening, are lower than those predicted by  
712 Byerlee's friction, and within the same order of magnitude as the values measured during the  
713 experiments during Stage III.

714

715

716

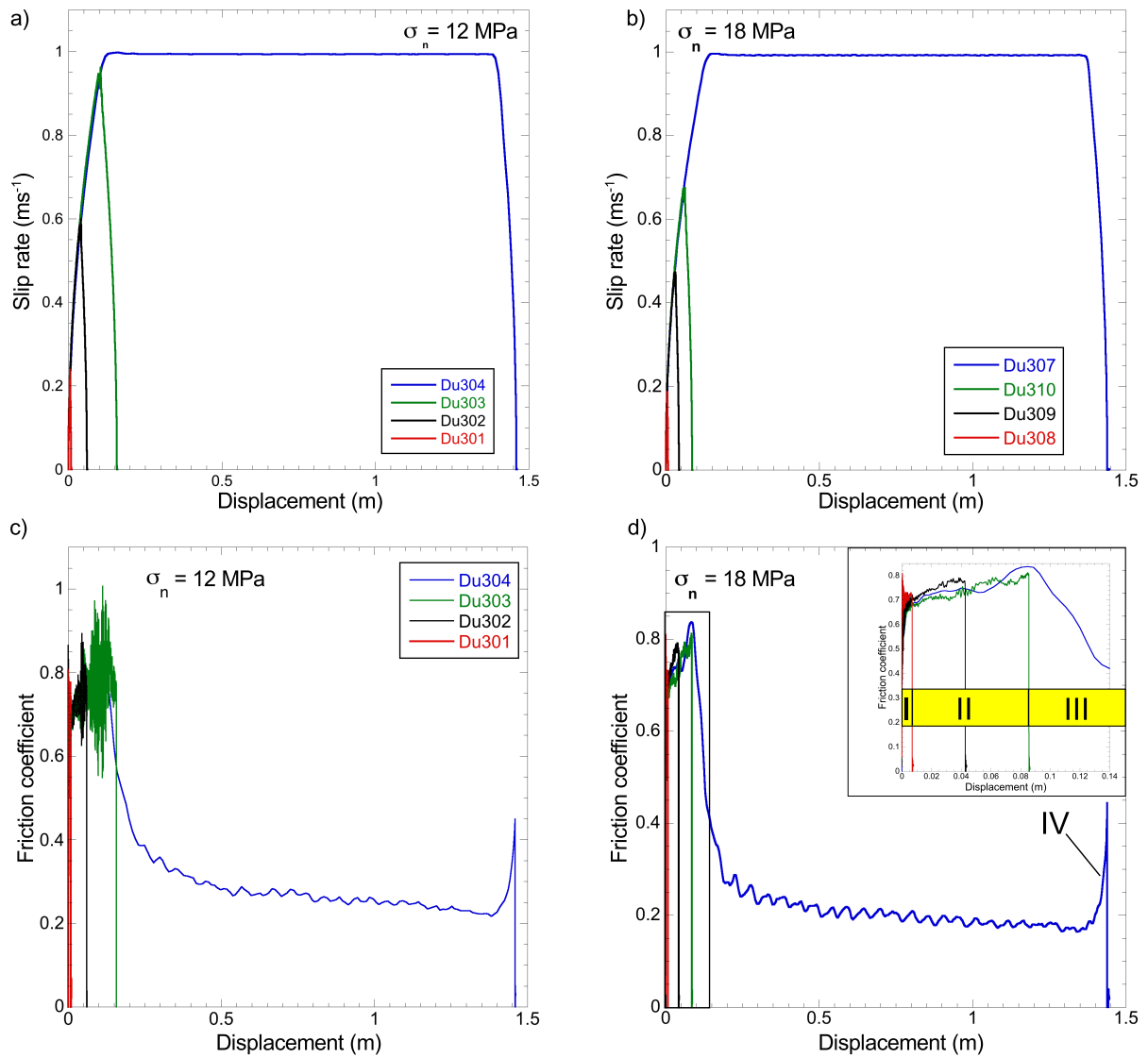
717

718

719

720

721



722

723 Figure 1

724

725

726

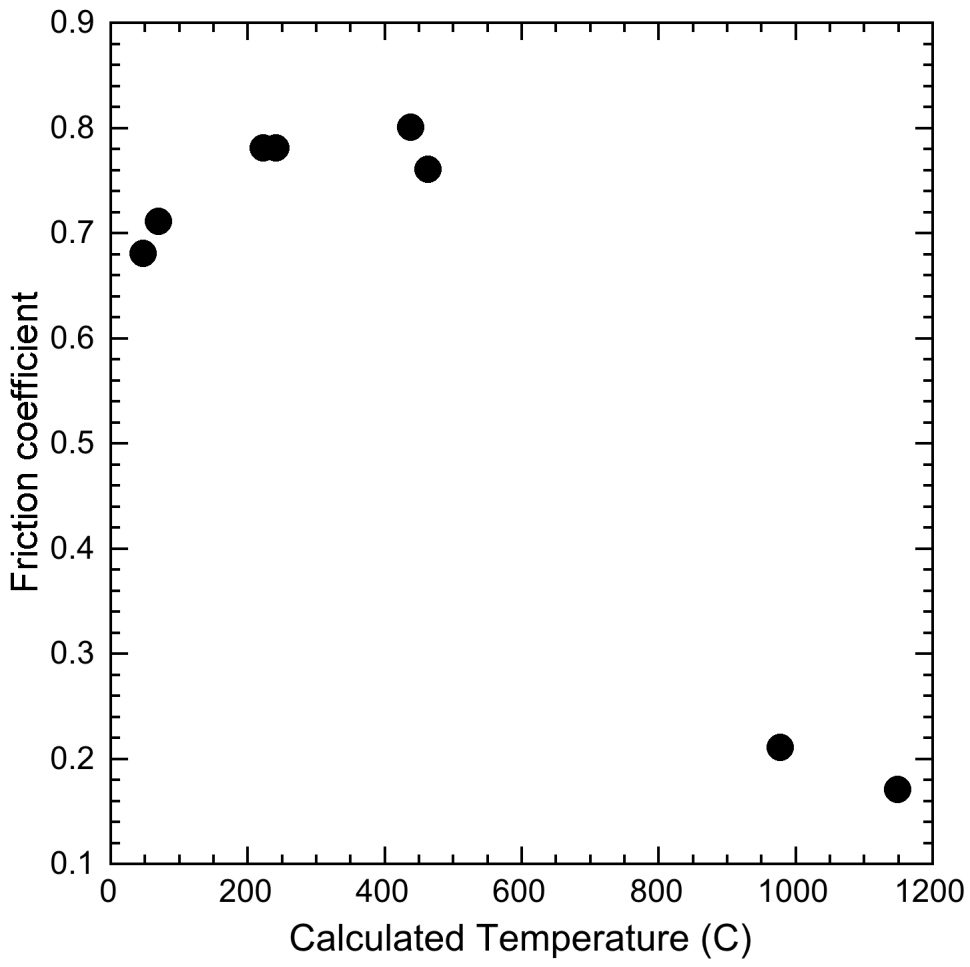
727

728

729

730

731



732

733 Figure 2

734

735

736

737

738

739

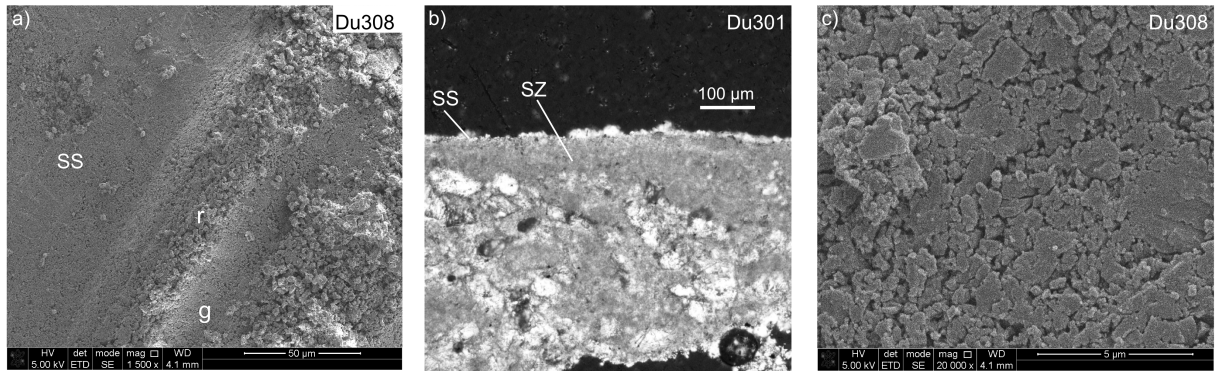
740

741

742

743

744



745

746 Figure 3

747

748

749

750

751

752

753

754

755

756

757

758

759

760

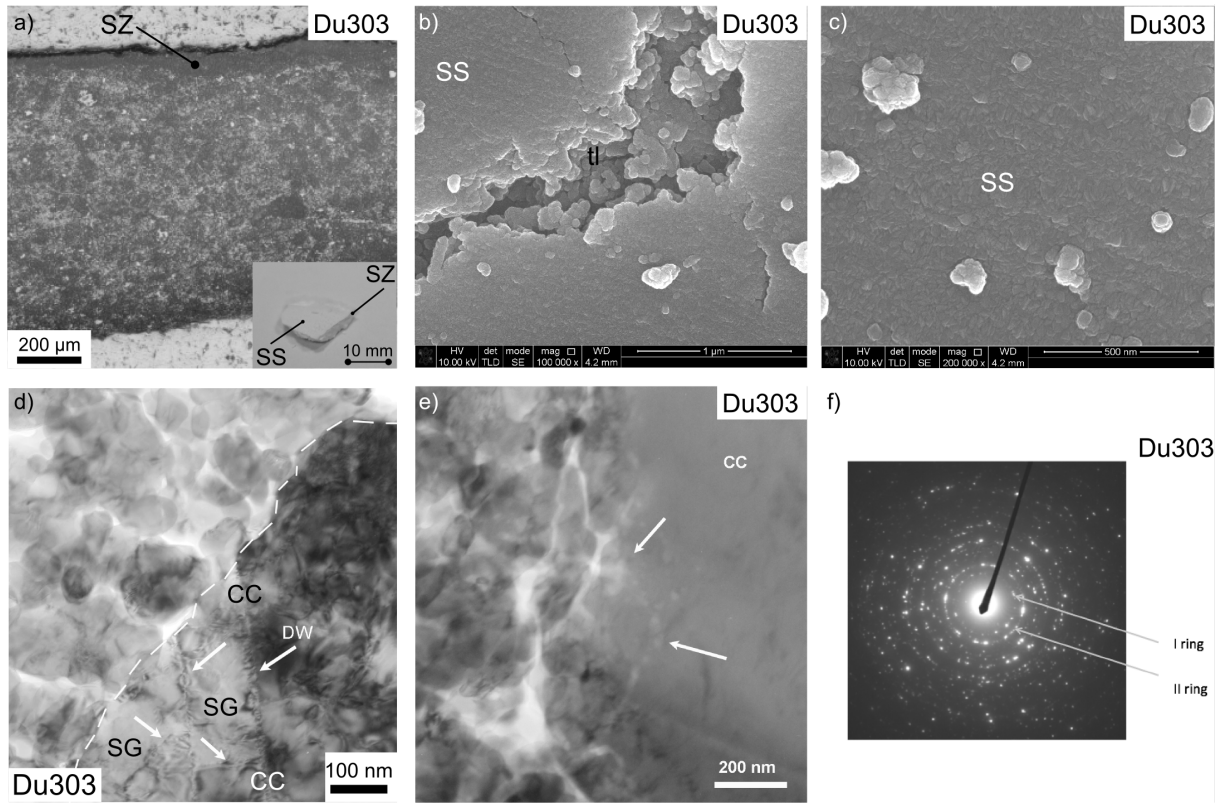
761

762

763

764

765



766

767 Figure 4

768

769

770

771

772

773

774

775

776

777

778

779

780

781

782

783

784

785

786

787

788

789

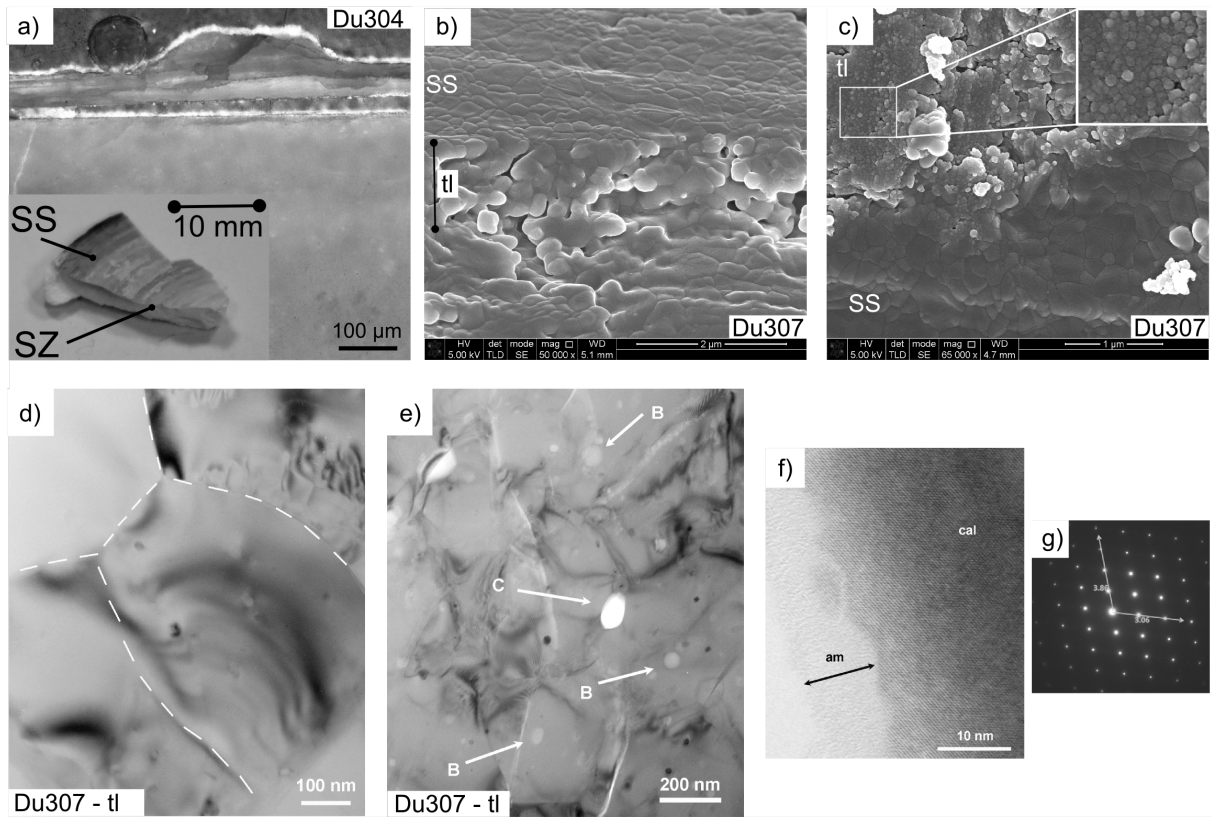
790

791

792

793

794



795  
796  
797  
798  
799  
800  
801  
802  
803  
804  
805  
806  
807  
808  
809  
810  
811  
812  
813  
814  
815  
816  
817  
818  
819  
820  
821  
822  
823

Figure 5

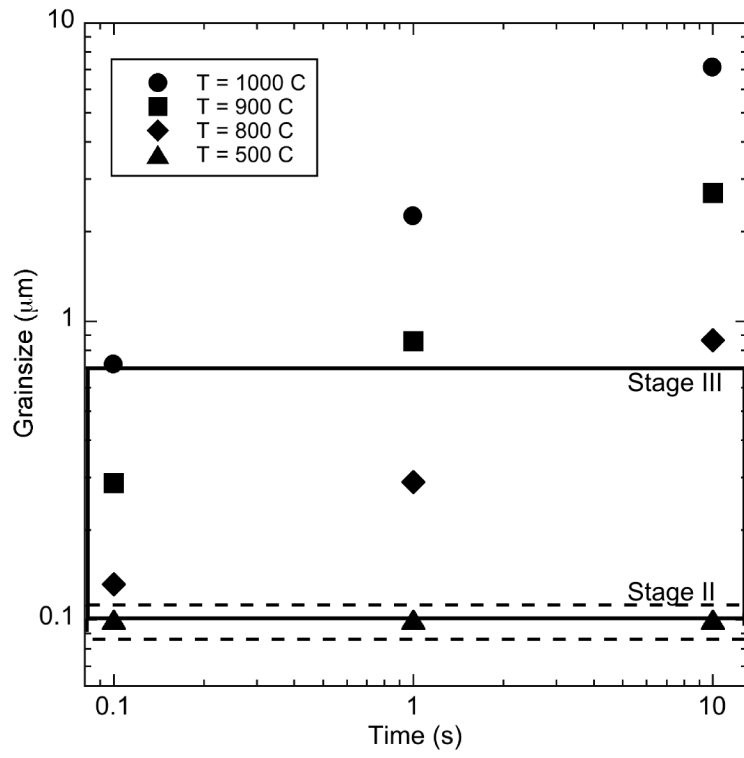
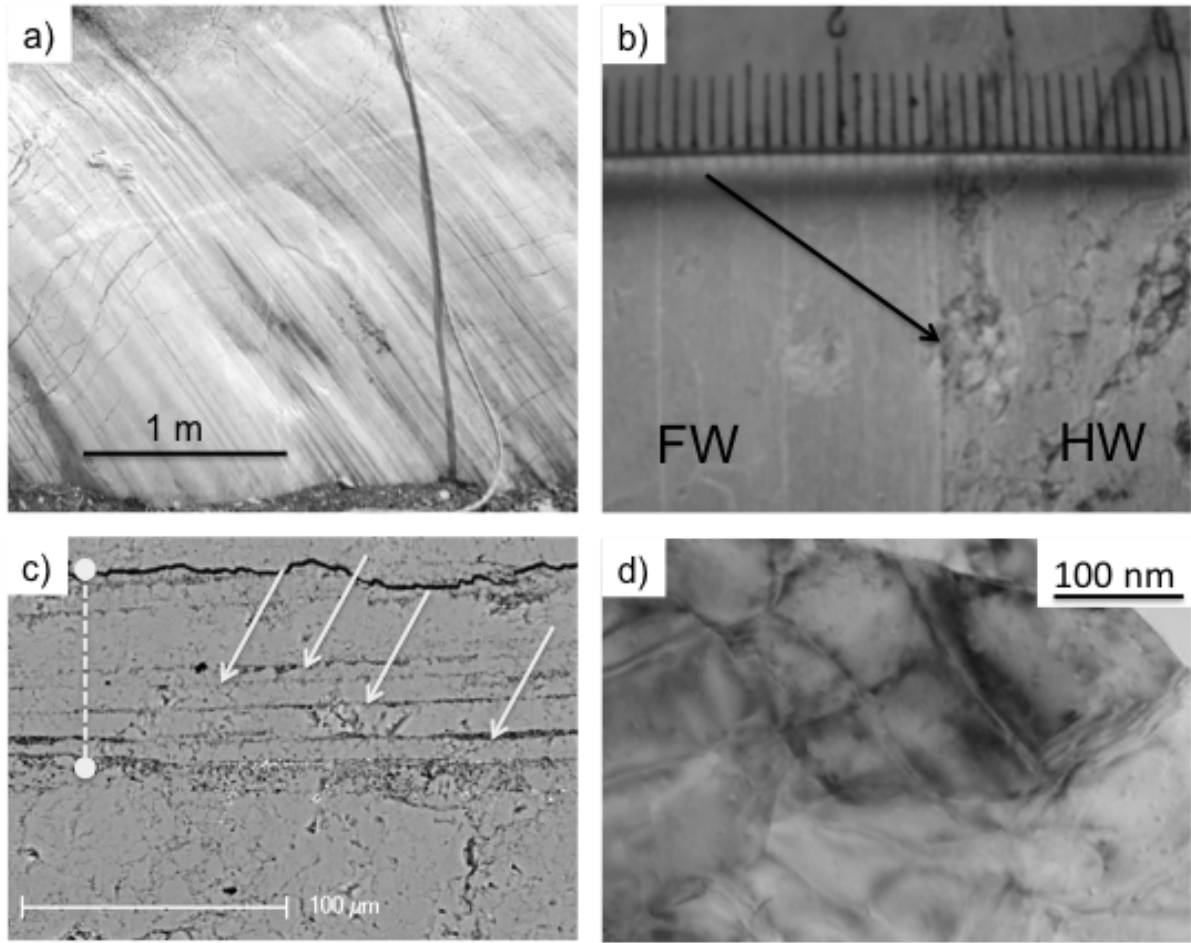


Figure 6

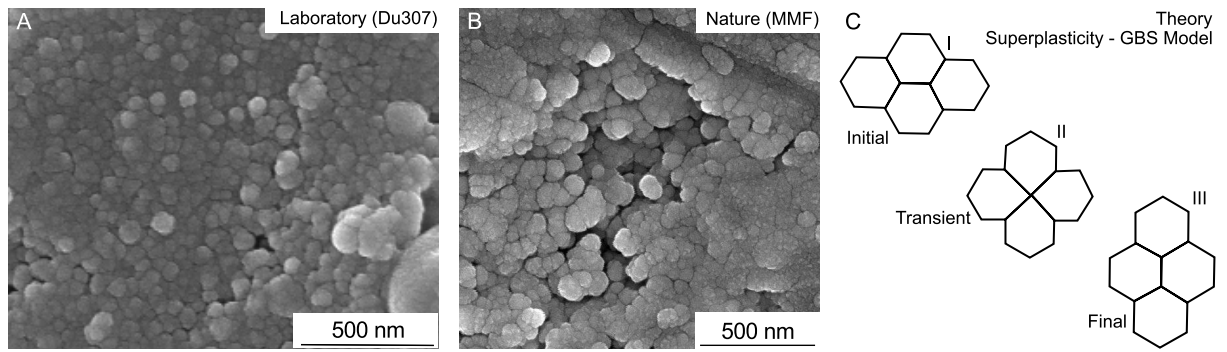
824  
 825  
 826  
 827  
 828  
 829  
 830  
 831  
 832  
 833  
 834  
 835  
 836  
 837  
 838  
 839  
 840  
 841  
 842  
 843  
 844  
 845  
 846  
 847  
 848  
 849  
 850  
 851  
 852  
 853  
 854





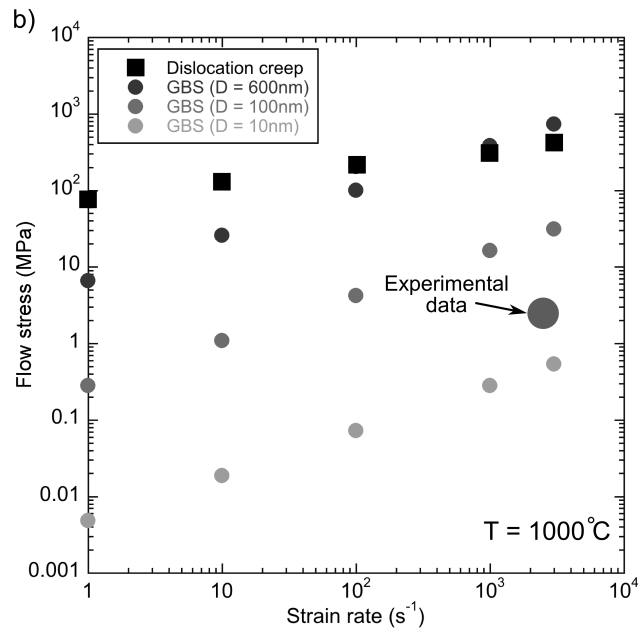
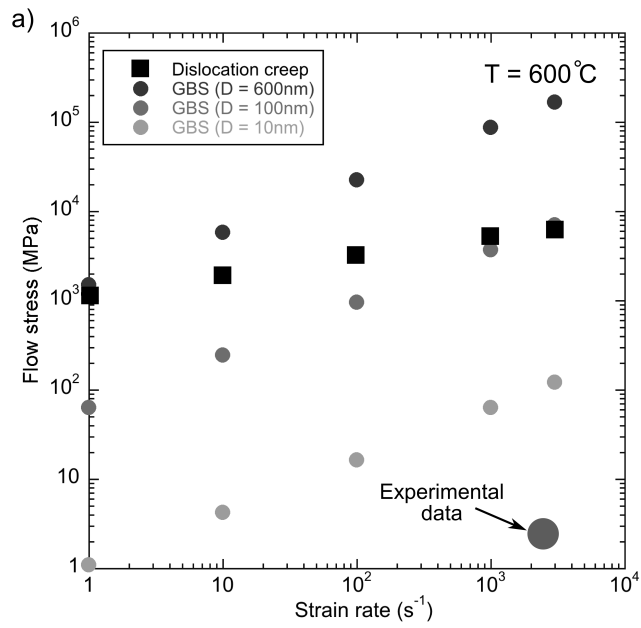
855  
856  
857  
858  
859  
860  
861  
862  
863  
864  
865  
866  
867  
868  
869  
870  
871  
872  
873  
874  
875  
876  
877  
878  
879

Figure 7



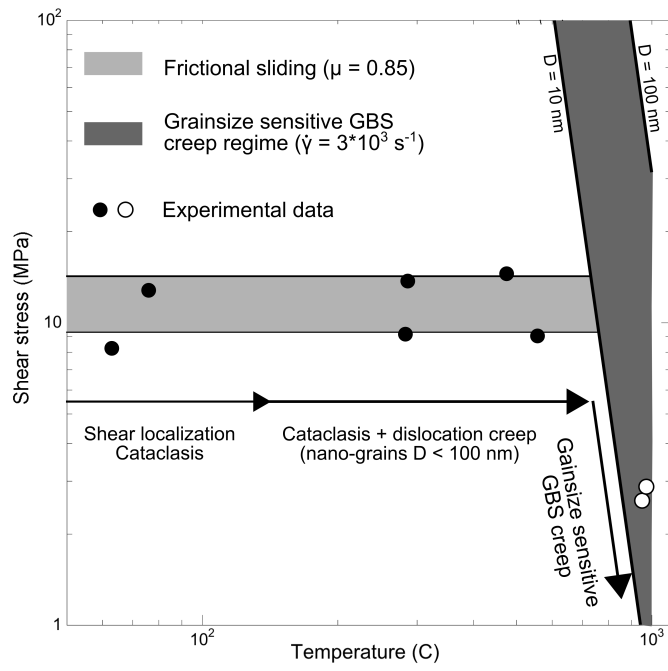
880  
 881  
 882  
 883  
 884  
 885  
 886  
 887  
 888  
 889  
 890  
 891  
 892  
 893  
 894  
 895  
 896  
 897  
 898  
 899  
 900  
 901  
 902  
 903  
 904  
 905  
 906  
 907  
 908  
 909  
 910  
 911  
 912  
 913  
 914  
 915  
 916  
 917  
 918  
 919  
 920  
 921

Figure 8



922  
 923  
 924  
 925  
 926  
 927  
 928  
 929  
 930  
 931  
 932  
 933  
 934  
 935  
 936  
 937

Figure 9



938  
939  
940

Figure 10